EFFECTS OF MICROSTRUCTURES ON THE SPATIOTEMPORAL CHARACTERISTICS OF TURBULENT FLOW SEPARATION AROUND RECTANGULAR PRISM

Fati Bio Abdul-Salam
Department of Mechanical Engineering
University of Manitoba
Winnipeg, MB R3T 5V6, Canada
abdulsa8@myumanitoba.ca

Mark F. Tachie
Department of Mechanical Engineering
University of Manitoba
Winnipeg, MB R3T 5V6, Canada
mark.tachie@umanitoba.ca

ABSTRACT

Time-resolved particle image velocimetry (TR-PIV) is used to experimentally investigate the turbulent separation induced by a rectangular prism with different microstructures. The Reynolds number based on the freestream velocity and thickness of the prism was 10000. Microstructures with two different morphologies, V-shaped riblets, arranged longitudinal (LG) and transverse (TR) to the flow direction and micropillars (MP) are tested and compared with a smooth (SM) surface. The results are analysed using the streamwise mean velocity, turbulence kinetic energy, frequency spectra, and reverse flow area. The results show a significant decrease in the reattachment length of the separation bubble over the surface of the micropillars case compared to the other test cases, but the wake bubble is independent of the surface structure. Contours of the turbulent kinetic energy show higher intensity but confined toward the micropillar prism compared to the other test cases. The Kelvin Helmholtz instability is amplified and occurs closer to the leading edge for the micropillars case. In contrast, the wake vortex shedding frequency is comparable for all test case. Analysis of the reverse flow area show that it is characterized by the low-frequency flapping motion.

INTRODUCTION

Flow separation induced by bluff bodies is a common phenomenon encountered in many engineering applications and can result in either beneficial or adverse effects depending on the area of application. In fluid-thermal systems, flow separation and its associated high turbulence levels are exploited to enhance mixing and convective heat transfer. On the other hand, the formation of unsteady recirculation region and vortex shedding could lead to structural resonance, increased drag, acoustic noise, and fatigue failure. Therefore, understanding the dynamics of flow separation and investigating effective methods to control it is of great importance for both engineering application and scientific research.

Several methods have been developed to control flow separation. These methods are classified into active and passive control methods. Active control, such as surface blowing and suction and synthetic jets, is highly effective in modifying flow separation, however, it requires addition of energy and complex devices. For passive control, on the other hand, the flow can be manipulated by changing the surface structures and properties, without requiring external energy input, and examples include microstructures and superhydrophobic surfaces. The use of microstructures to control flow separation is inspired by nature. Aquatic creatures, particularly sharks, have received significant attention from researchers due to their exceptional swimming speed and hydrodynamic performance. Microscopic examinations of the dermal scales of shark skin have revealed distinct riblet-like structures (Motta et al., 2012), and it has been shown that the morphology, orientation, spacing, and height play a crucial role in modifying the flow dynamics. Microstructures can also be considered as roughness elements, which are common in diverse applications such as corroded bridge piers and on ice booms affected by ice accumulation and abrasion. Evans et al. (2018) investigated the effects of cylindrical pillars with diverging tips on separated flows and found that the microstructures reduced the separation bubble but did not increase the production of turbulent kinetic energy. Du et al. (2024) studied the effect of microstructure height on the separated flow over a rectangular prism and found no significant change in the separation bubble when the ratio of the height of microstructure to thickness of the prism was less than 0.03. However, as the ratio increases beyond 0.03, the bubble size decreased. While these studies have improved our understanding on the effects of microstructures on separated flows, the influence of different microstructures morphologies on the spatiotemporal characteristics of flow around bluff bodies with fixed separation point is not fully understood.

The goal of this study is to investigate the influence of different microstructures on the flow separation induced by a sharp-edged rectangular prism. The surface of the prism is modified with microstructures with two different morphologies, V-shaped riblets and micropillars. The prism with a smooth surface is also investigated as a reference test case.

EXPERIMENTAL SET-UP

The experiments were conducted in an open recirculating water channel at the University of Manitoba. The streamwise length, vertical height and spanwise width of the channel are 6000 mm, 450 mm, and 600 mm, respectively. A rectangular prism with vertical height, h = 20 mm, streamwise length, L = 180 mm, and spanwise, B = 588 mm was used. The corresponding aspect ratio (L/h) of the prism is 9, which is sufficient to ensure permanent reattachment of the separated shear layer onto the prism surface. The microstructures were arranged at the top and bottom surfaces of the prisms, and a 5 mm distance was ensured between the leading edge and the first row of microstructures. The height of the microstructures is 1.5 mm. The spacing of the V-shaped riblet is 3 mm and are arranged in two configurations: longitudinal to the flow direction (LG) and transverse to the flow direction (TR) as shown in Figure 1. The streamwise and spanwise dimensions of the micropillars (MP) is 0.8 mm and 2.0 mm, respectively, with spacings of 1.5 mm in the streamwise direction and

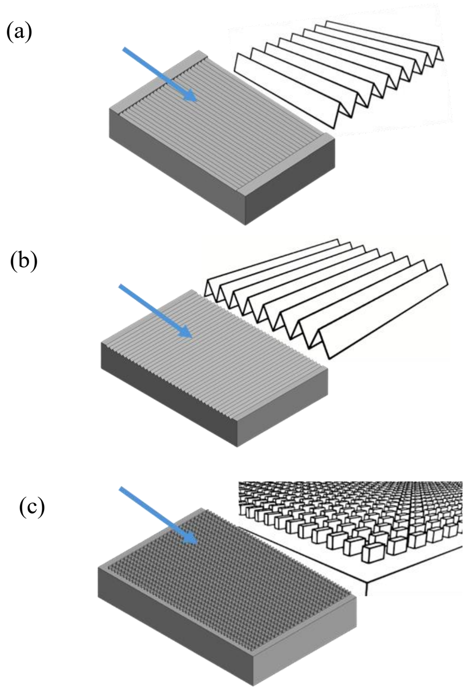

Figure 1: Schematic and cross-sectional view of (a) LG, (b) TR, and (c) MP.

1.0 mm in the spanwise. The freestream velocity was set to 0.5 m/s and the Reynolds number based on the height of the prism was 10000.

Velocity measurements were performed at the mid-span of the channel using a time-resolved particle image velocimetry. Silver coated hollow glass spheres with mean diameter of 10 μm and specific gravity of 1.4 was used to seed the water. The flow was illuminated with a diode pumped dual-cavity dual-head high speed Neodymium-doped yttrium lithium fluoride (Nd:YLF) laser. Two high-speed 12-bit complementary metal oxide semiconductor cameras, with resolution of 2560 pixel × 1600 pixel were arranged side by side to image the flow. The first camera was fitted with a Sigma 105 mm lens, to provide higher spatial resolution to adequately resolve the dynamics of the shear layer and the second camera was fitted with a Nikon 60 mm lens. The dimensions of the first field of view (FOV) were $6.0h \times 3.8h$ in the streamwise and vertical direction, respectively, and the second FOV were $14.3h \times 8.9h$. The sampling frequency was set to 800 Hz and 60000 images were captured for each test case. Data acquisition, image processing, and velocity vector calculations were done using a commercial software supplied by LaVision, Inc. A GPU-accelerated multi-pass cross-correlation algorithm with an initial interrogation window of 128 pixel × 128 pixel with 50% overlap and four additional passes with interrogation window of 24 pixel × 24 pixel with 75% overlap was used for velocity vector calculations.

RESULTS AND DISCUSSION

Mean flow characteristics and Turbulent Kinetic Energy

Contours of the streamwise mean velocity (U) superimposed with mean streamlines are presented in Figure 2(a-d) to examine the effects of surface modification on the mean flow topology. The isopleth of $U = 0$ is used to demarcate the recirculation regions and identify the mean reattachment points. The approach flow separates at the sharp leading edge and accelerates over the prism, resulting in a

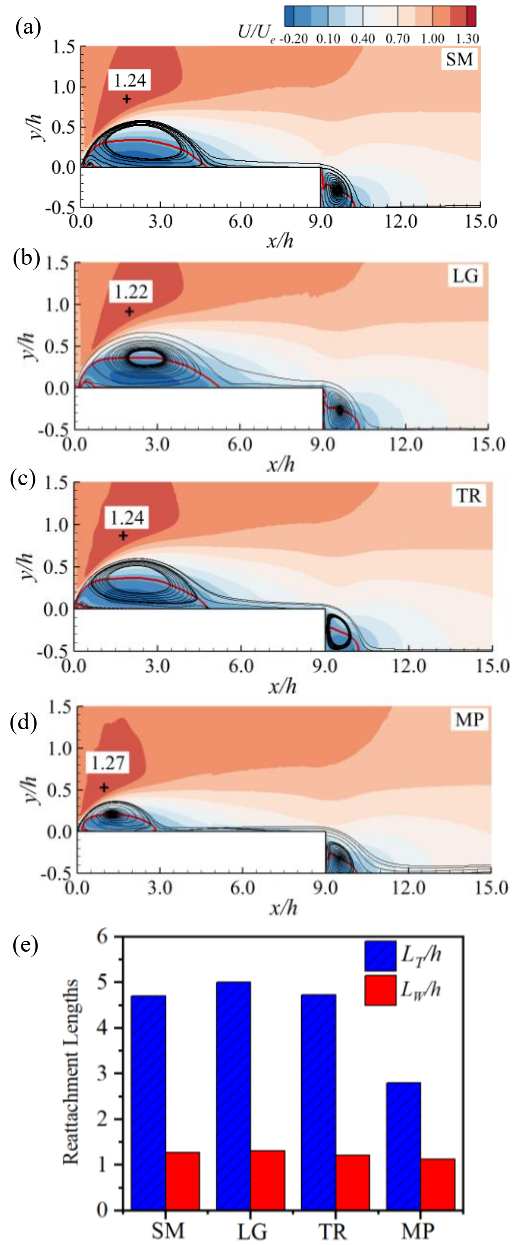

Figure 2: Contour of the streamwise mean velocity for (a) SM, (b) LG, (c) TR, (d) MP, and (e) the reattachment lengths over and recirculation in the wake of the prisms.

local maximum velocity. The maximum values of mean velocity ($1.22U_\infty$−$1.27U_\infty$) is not significantly affected by the surface condition, however, the magnitude of the maximum mean reverse flow in the micropillar test case ($0.24U_\infty$) is 22.6% smaller than that in the SM, LG, and TR cases ($0.31U_\infty$). The mean streamlines reveal two distinct recirculation bubbles formed over and in the wake of the prisms, hereby referred to as the primary and wake vortices, respectively. Near the leading edge, a relatively small secondary recirculation bubble that counter rotates with respect to the primary vortex is formed. The secondary vortex is formed due to an adverse pressure gradient induced by the decelerating reverse flow within primary vortex. The secondary bubble is present for the smooth and riblet test cases. However, for the micropillar test case the the secondary vortex is suppressed due to the reduced streamwise deceleration of the near-wall mean flow. This reduction weakens the local adverse pressure gradient required for the formation of the secondary vortex. The reattachment lengths over the surface of the prism (L_T), defined as the streamwise distance from the leading edge to the point of intersection of $U = 0$ on the surface of the prism, and recirculation lengths in the wake (L_W), defined as the streamwise distance from the trailing edge to the saddle point, presented in Figure 2(e) are used to examine the effects of surface modification on the recirculation bubbles. The mean reattachment length of the primary vortex over the smooth prism case is L_T = 4.7h. Previous studies have shown that the reattachment length for rectangular prisms with $L/h \geq 5$ with smooth surface is between 4h to 5h, provided the Reynolds number is on the order of 10^4 (Kiya and Sasaki, 1983; Taylor et al., 2014; Moore et al., 2019). Hence, the present result is in good agreement with values reported in the literature. From Figure 2(e), no significant change in L_T is observed for the two riblet test cases, and it is comparable to the smooth test case. However, the micropillars significantly suppresses the recirculation region, showing a 40% reduction compared to the other test cases. In the wake region, the recirculation length is independent of the surface modification ($L_W \approx 1.2h$). The wake recirculation length is consistent with the values reported in previous studies for rectangular prisms with L/h = 9 (Shi et al., 2010; Liu and Zhang, 2015).

The effect of surface modification on the behaviour of the separated shear layer is analyzed using the turbulent kinetic energy (TKE). The TKE is estimated as TKE = $0.5(\overline{u'u'} + \overline{v'v'})$, where $\overline{u'u'}$ and $\overline{v'v'}$ are the streamwise and vertical Reynolds normal stresses, respectively, since the spanwise velocity was not measured. Contours of the TKE superimposed with the trajectory of the separated shear layer are presented in Figure 3. Following Moore et al. (2019), the average trajectory of the shear layer is defined using the locus of the maximum turbulent kinetic energy values. Regardless of the test case, elevated regions of TKE are localized along the separated shear layer indicating the initiation and saturation of turbulence therein. The intensity and spatial extent of this region are comparable for the smooth and riblet test cases. In contrast, the micropillar test case exhibits increased intensity and reduced spatial extent. This indicates that the micropillars promote stronger velocity fluctuations and enhance flow entrainment in the upstream region. In the wake region, elevated TKE regions are observed along the centreline and are primarily contributed by the vertical Reynolds normal stress. This is attributed to the alternating shedding of vortices of opposite sign and equal strength (Alves Portela et al., 2017; Abdul-Salam et al., 2024). As shown in the figures, the average position of the shear layer initially moves away from the surface of the prism in the first half of the recirculation region and remains approximately constant downstream of its centre. Similar observations were made by Kiya and Sasaki (1983) and Moore et al. (2019). The variation of the shear layer trajectory is similar for the smooth and riblet test cases, which is consistent with the similar reattachment lengths reported in Figure 2(e). The difference between the asymptotic value of the mean shear layer position of the micropillar case compared to the other test cases is approximately 0.2h. This shows that the micropillars significantly affect the turbulence structures within the recirculation bubble.

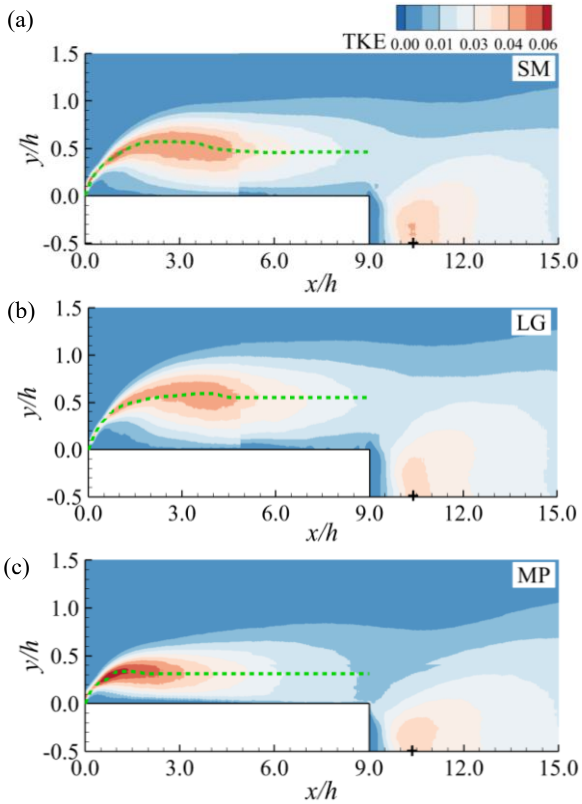

Figure 3: Contours of the turbulent kinetic energy superimposed with the trajectory of the shear layer (green dashed lines) for (a) SM, (b) LG, and (c) MP.

Frequency spectra and reverse flow area

Flow separation induced by rectangular prisms in a uniform are characterized by three main instabilities: Kelvin Helmholtz (KH) instability, von Kármán (VK) vortex shedding, and low-frequency flapping motion (Abdul-Salam et al., 2024; Cimarelli et al., 2024). The effects of surface modification on these instabilities are investigated in the following section.

Due to their convective nature, the KH vortices can only be detected downstream of their origin. Figure 4 presents representative snapshots of instantaneous spanwise vorticity to visualize the KH instability. The figures clearly show the typical transition process. The separated shear layer is initially laminar immediately downstream the separation point. Shortly downstream, it becomes unstable and rolls up into discrete KH vortices (indicated by the red arrows). In the micropillar case, the onset of instability occurs closer to the leading edge indicating earlier transition to turbulence.

The frequency spectra of the velocity fluctuations are presented in Figures 5 and 6 to determine the VK and KH frequencies, respectively. The spectra of the vertical velocity fluctuation at the location of maximum turbulent kinetic energy in the wake region is used to determine the wake frequency. Regardless of the test case, a distinct dominant peak is observed at St_{VK} (= $f_{VK}h/U_e$, where f_{VK} is the VK frequency) of 0.17, suggesting that the microstructures have negligible influence in the wake frequency. This value is in good agreement with previous studies for rectangular prism with L/h = 9 (Ohya et al., 1989; Liu and Zhang, 2015; Zhang and Liu, 2012).

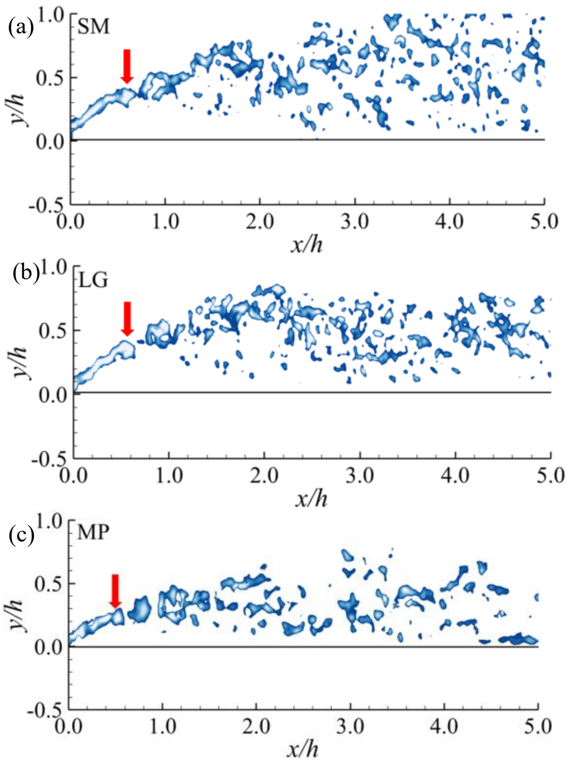

Figure 4: Representative snapshots of instantaneous spanwise vorticity for (a) SM, (b) LG and (c) MP.

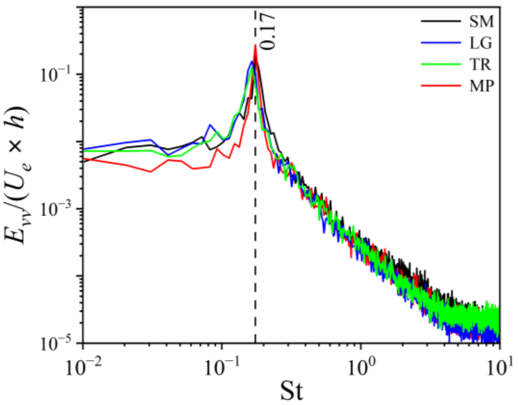

Figure 5: Frequency spectra at the location of maximum turbulent kinetic energy in the wake region.

Figure 6 presents the spectra of the streamwise velocity fluctuation at selected locations along the shear layer to determine the KH frequency. Near the leading edge (x/h = 0.05), the spectra reveal peaks at Strouhal numbers of less than 0.13, regardless of the test. This observation contrasts with previous studies by Moore et al. (2019) and Kumahor and Tachie (2023) for prisms with $1 \leq CR \leq 5$, where the dominant VK shedding frequency is evident near the leading edge. As shown by Lander et al. (2018) and Moore et al. (2019), the KH frequency manifests as broadband peaks at higher frequency relative to the VK frequency as the separated flow transitions from laminar to turbulent. For the smooth test case, the broadband peak is first detected at $x/h = 0.53$ with a peak value of St_{KH} (= $f_{KH}h/U_e$, where f_{KH} is the KH frequency) of 1.92. This peak broadens and shifts towards lower frequencies as the shear layer evolves downstream due to the vortex pairing mechanism (Moore et al., 2019; Fang et al., 2022). A similar trend is observed for the longitudinal test case, where the broadband peak is first detected at $x/h = 0.55$ but with a slightly lower frequency value of $St_{KH} = 1.63$. For the micropillar, transition to turbulence in the shear layer occurs earlier, at $x/h = 0.44$, with a corresponding St_{KH} of 2.36. Although not shown, the KH frequency for the transverse is 1.90. The comparatively higher KH frequency observed for the micropillar test case indicates a more rapid growth of the leading-edge vortices.

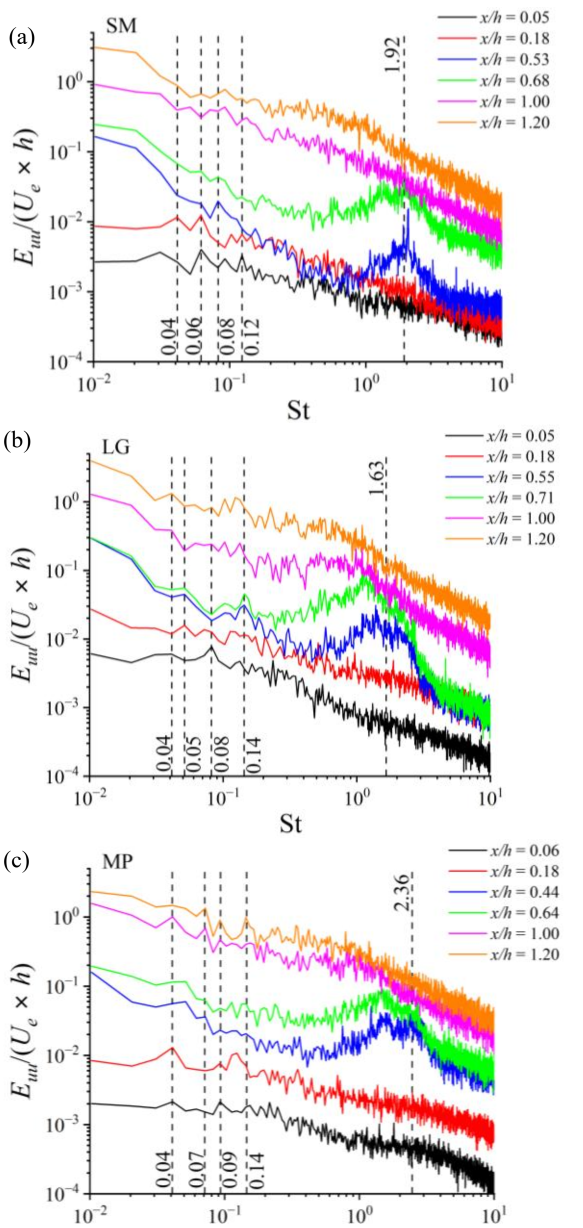

Figure 6: Frequency spectra along the shear layer for (a) SM, (b) LG, and (c) MP.

The spectra of the streamwise velocity fluctuations (E_u) along the flow at y/h = 0.1 are shown in Figure 7 to investigate the influence of surface modification in the near-wall region. It is noted that similar analysis was performed at y/h = 0.05 and the results are comparable. Elevated regions of E_u concentrate at multiple bands, showing the multi-scale nature of separating flows. Regardless of the surface condition, the dominant frequencies over the surface of the prisms are at *St*

≤ 0.05. For the smooth and riblet test case, the dominance of the low frequency initiates close to the reattachment point and persists up to the trailing edge of the prism. However, the energy content is more pronounced and broaden for the longitudinal riblet. Meanwhile, for the micropillars, although the low frequency also initiates close to the reattachment point, the energy contents are significantly low. In the wake region, a dominant peak is observed at a Strouhal number of 0.17, which is attributed to the wake vortex shedding frequency and is more energetic for the micropillars indicating more organized vortices. For the smooth and riblets test cases, additional frequencies are observed at $St \approx 0.053$ and are more pronounced for the riblets. This feature is also present for the micropillars case, but the amplitude is significantly weak.

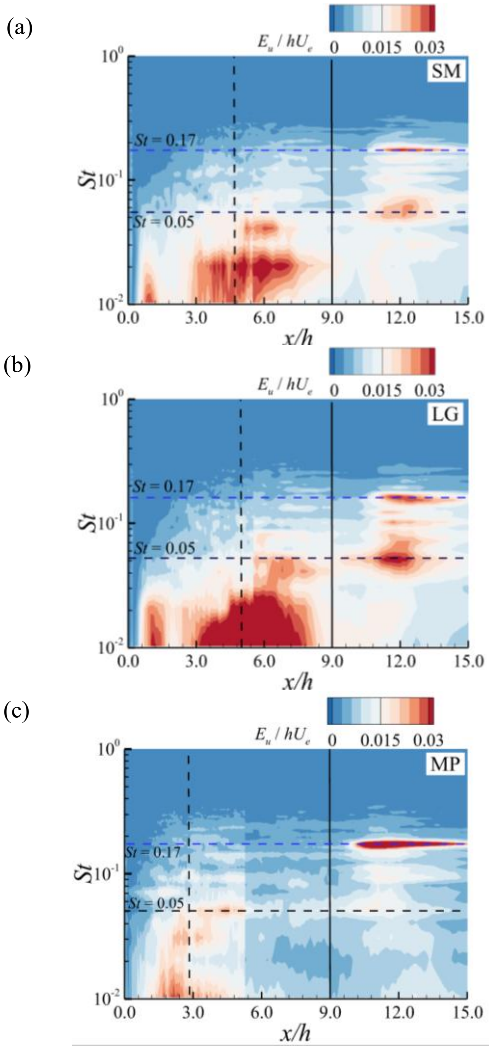

Figure 7: Spectra contour of the streamwise fluctuating velocity at the $y/h = 0.10$ for (a) SM, (b) LG, and (c) MP. The dashed and solid vertical lines represent the mean reattachment length and trailing edge, respectively.

Following Pearson et al. (2013) and Fang et al. (2022), the flapping motions (expansion/shrinkage) of the separated shear layers over the surface of the prisms are investigated using the temporal variations of the reverse flow area. Figure 8 presents instantaneous snapshots of the reverse flow region to visualize the flow. Results are presented for the smooth and micropillar test cases for brevity. Figures 8(a,b) show typical instantaneous reverse flow region for the smooth prism. The smaller reverse flow region in Figure 8(a) and larger region in Figure 8(b), correspond to instances of contraction and expansion of recirculation region, respectively. Similarly, Figures 8(c,d) show instances of contraction and expansion, respectively, for the micropillar test case. The contrast in the recirculation regions between the two test cases is immediately apparent. The reverse flow region in the micropillar test case is significantly reduced compared to the smooth test case. The is consistent with the small size of the recirculation bubble for the MP test case shown in Figure 2.

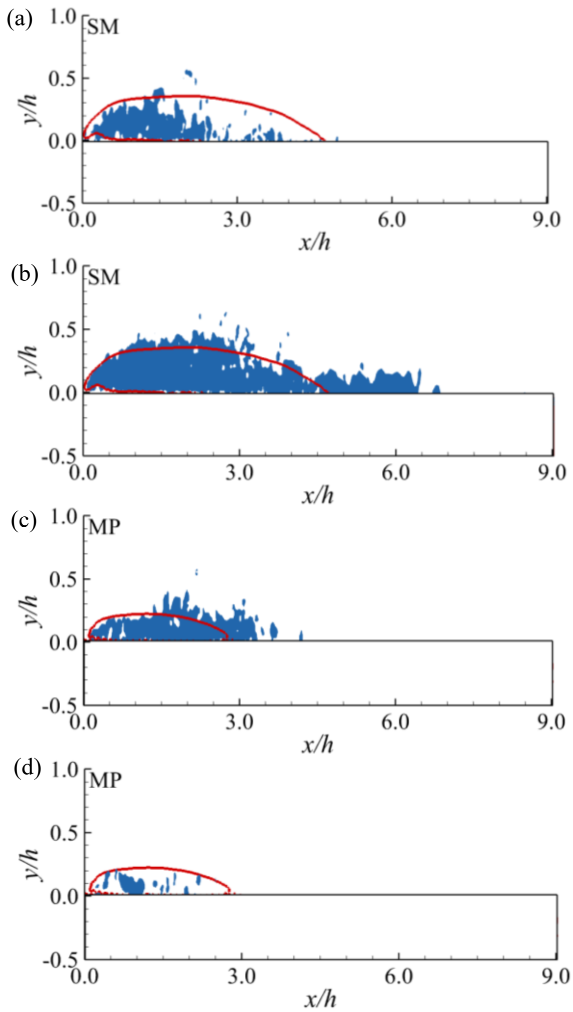

Figure 8: Contours of instantaneous reverse flow regions superimposed with the isopleth of $U = 0$ for (a), (b) SM and (c), (d) MP.

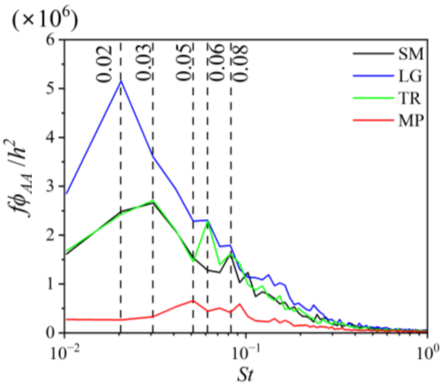

Figure 9: Frequency spectra of the reverse flow area.

To determine the size of the instantaneous separation bubble, the reverse flow area is calculated by summing all regions where $u < 0$ within the region of interest. The analysis is performed for $x/h \times y/h \in [0.0,\ 9.0] \times [0.0, 1.5]$. The average reverse flow areas ($\bar{A}/h^2$) are 1.25, 1.48, 1.32, and 0.47, for SM, LG, TR, and MP, respectively. The frequency spectra are presented in Figure 9 to determine the flapping motion frequencies. The spectra show dominant peaks at St_{FM} (= $f_{FM}h/U_e$, where f_{FM} is the flapping motion frequency) of 0.03, 0.02, 0.03, and 0.05, for SM, LG, TR, and MP, respectively. These correspond to St_{LT} = 0.15, 0.11, 0.15, and 0.14, respectively, and fall within the range associated with the low-frequency flapping motion of separation bubbles (St_{LT} = 0.08 – 0.20) reported in the literature (Kiya and Sasaki, 1983; Fang et al., 2022; Abdul-Salam et al. 2024).

SUMMARY AND CONCLUSION

Turbulent flow separation over rectangular prisms with different surface modifications was studied using a time-resolved particle image velocimetry. Two different surface configurations, V-shaped riblets, arranged longitudinal (LG) and transverse (TR) to the flow direction and micropillars (MP), as well as a reference smooth surface (SM) were tested. The Reynolds number based on the freestream velocity and prism thickness was 10000 and the streamwise aspect ratios of the prisms were 9.

The results indicate that the maximum mean reverse flow and mean reattachment length are similar for the smooth and riblet cases, whereas the micropillar configuration reduces these parameters by 23% and 40%, respectively. In contrast, the wake recirculation length is independent of the surface condition. Elevated turbulent kinetic energy (TKE) is observed along the separated shear layer. For the smooth and riblet test cases, both the intensity and spatial extent are comparable. In the micropillars test case, TKE becomes more intense but confined towards the prism.

Frequency spectra analysis of the velocity fluctuations reveal that the Kelvin-Helmholtz instability is higher for the micropillar test case and occurs closer to the leading edge compared to the smooth and riblet test cases. The von Kármán frequency, in contrast, is independent of the surface condition. The frequency of the flapping motion, which was determined as the dominant frequency of the reverse flow area over the surface of the prisms is St_{LT} = 0.15, 0.11, 0.15, and 0.14, for the smooth, longitudinal riblet, transverse riblet, and micropillars, respectively. The flapping frequency is consistent with those reported in the literature.

ACKNOWLEDGEMENTS

The authors are grateful to the Natural Sciences and Engineering Research Council of Canada (NSERC) and the Canada Foundation for Innovation (CFI) for their financial support to M.F.T.

REFERENCES

Abdul-Salam, F. B., Fang, X., and Tachie, M. F., 2024, "Influences of blockage ratio and Reynolds number on the spatiotemporal dynamics around a rectangular prism", *Physics of Fluids*, 36, 105198.

Alves Portela, F., Papadakis, G., and Vassilicos, J. C., 2017, "The turbulence cascade in the near wake of a square prism", *Journal of Fluid Mechanics*, Vol. 825, pp. 315- 352.

Cimarelli, A., Corsini, R., and Stalio, E., 2024, "Reynolds number effects in separating and reattaching flows with passive scalar transport", Journal of Fluid Mechanics, 984, A20.

Du, Z., Gao, A., You, C., Chen, G., Liu, Y., Li, H., Lv, P., and Duan, H., 2024, "Regulating turbulent separation by surface microstructures on a blunt plate", *Physics of Fluids*, Vol. 36, 052109.

Evans, B. H., Ali, M. H., Gorumlu, S., Doosttalab, A., Aksak, B., Chamorro, L. P., and Castillo, L., 2012, "Engineered bio-inspired coating for passive flow control", *Proceedings of the Nation Academy of Sciences of the United States of America*, Vol. 115, pp. 1210- 1214.

Fang, X., Tachie, M. F., and Dow, K., 2022, "Turbulent separations beneath semi-submerged bluff bodies with smooth and rough undersurface", *Journal of Fluid Mechanics*, 947, A19.

Kiya, M., and Sasaki, K., 1983, "Freestream turbulence effects on a separation bubble", *Journal of Wind Engineering and Industrial Aerodynamics*, Vol. 14, pp. 375- 386.

Kumahor, S., and Tachie, M. F., 2023, "Effects of streamwise aspect ratio on the spatio-temporal characteristics of flow around rectangular cylinders", *International Journal of Heat and Fluid Flow*, Vol. 101, 109133.

Lander, D. C., Moore, D. M., Letchford, C. W., and Amitay, M., 2018, "Scaling of square-prism shear layers", *Journal of Fluid Mechanics*, Vol. 849, pp. 1096- 1119.

Liu, Y., and Zhang, Q., 2015, "Dynamic mode decomposition of separated flow over a finite blunt plate: Time-resolved particle image velocimetry measurements", *Experiments in Fluids*, 56 (7).

Moore, D. M., Letchford, C. W., and Amitay, M., 2019, "Energetic scales in a bluff body shear layer", *Journal of Fluid Mechanics*, Vol. 875, pp. 543- 575.

Motta, P. J., Habegger, M. L., Lang, A., Hueter, R. E., and Davis, J., 2012, "Scale morphology and flexibility in the shortfin *mako Isurus oxyrinchus* and the blacktip shark *Carcharhinus limbatus*", *Journal of Morphology*, Vol. 273, pp. 1096- 1110.

Ohya, Y., Nakamura, N., Ozono, S., Tsuruta, H., and Nakayama, R., 1992, "A numerical study of vortex shedding from flat plates with square leading and trailing edges", *Journal of Fluid Mechanics*, Vol. 236, pp. 445- 460.

Shi, L.L., Liu, Y.Z., and Yu, J., 2010, "PIV measurement of separated flow over a blunt plate with different chord-to-thickness ratios", *Journal of Fluid and Structures*, 26 (4) pp. 644- 657.

Taylor, Z. J., Gurka, R., and Kopp, G.A., 2014, "Effects of leading edge geometry on the vortex shedding frequency of an elongated bluff body at high Reynolds numbers", *Journal of Wind Engineering and Industrial Aerodynamics*, Vol. 128, pp. 66- 75.